SMC-TR-99-07

AEROSPACE REPORT NO.
TR-98(1306)-5

Field Instrumentation for Atmospheric Plume and Contrail Measurements

20 August 1998

Prepared by

E. J. BEITING
Mechanics and Materials Technology Center
Technology Operations

Prepared for

SPACE AND MISSILE SYSTEMS CENTER
AIR FORCE MATERIEL COMMAND
2430 E. El Segundo Boulevard
Los Angeles Air Force Base, CA 90245

Corporate Business Division

THE AEROSPACE CORPORATION
El Segundo, California

This report was submitted by The Aerospace Corporation, El Segundo, CA 90245-4691, under Contract No. F04701-93-C-0094 with the Space and Missile Systems Center, 2430 E. El Segundo Blvd., Los Angeles Air Force Base, CA 90245. It was reviewed and approved for The Aerospace Corporation by S. Feuerstein, Principal Director, Mechanics and Materials Technology Center. Mr. John R. Edwards was the project officer.

This report has been reviewed by the Public Affairs Office (PAS) and is releasable to the National Technical Information Service (NTIS). At NTIS, it will be available to the general public, including foreign nationals.

This technical report has been reviewed and is approved for publication. Publication of this report does not constitute Air Force approval of the report's findings or conclusions. It is published only for the exchange and stimulation of ideas.

J. R. Edwards
SMC/AXFV

REPORT DOCUMENTATION PAGE

Form Approved
OMB No. 0704-0188

1. AGENCY USE ONLY (*Leave blank*)	2. REPORT DATE	3. REPORT TYPE AND DATES COVERED
	20 August 1998	

4. TITLE AND SUBTITLE
Field Instrumentation for Atmospheric Plume and Contrail Measurements

5. FUNDING NUMBERS
F04701-93-C-0094

6. AUTHOR(S)
E. J. Beiting

7. PERFORMING ORGANIZATION NAME(S) AND ADDRESS(ES)
The Aerospace Corporation
Technology Operations
El Segundo, CA 90245-4691

8. PERFORMING ORGANIZATION REPORT NUMBER
TR-98(1306)-5

9. SPONSORING/MONITORING AGENCY NAME(S) AND ADDRESS(ES)
Space and Missile Systems Center
Air Force Materiel Command
2430 E. El Segundo Boulevard
Los Angeles Air Force Base, CA 90245

10. SPONSORING/MONITORING AGENCY REPORT NUMBER
SMC-TR-99-07

11. SUPPLEMENTARY NOTES

12a. DISTRIBUTION/AVAILABILITY STATEMENT
Approved for public release; distribution unlimited

12b. DISTRIBUTION CODE

13. ABSTRACT (*Maximum 200 words*)

This report describes two ground-based field instruments that measured the expansion rate of solid rocket motor exhaust in the stratosphere. These instruments, however, are useful for atmospheric plume or contrail measurements in general because of their ability to enhance the contrast of such images against the bright sky. The first instrument records video images at SVHS resolution of polarized near-infrared light. The second instrument uses an electronic camera to record 1.6 million pixel still images with 10-bit gray-scale resolution of polarized light in a similar near-infrared spectral region. The cameras are mounted on tripods that automatically record the azimuth and elevation of the center of the field-of-view on the electronic image. The technique used to enhance the contrast of the image of the plume against the bright day sky is presented. The instruments were used successfully to observe plume expansion of Space Shuttle and Titan IV vehicles.

14. SUBJECT TERMS
Field Instrumentation, Atmospheric Plume Measurements, Contrail Detection, Remote Sensing, Environmental Measurements, Polarized Light Imaging.

15. NUMBER OF PAGES
27

16. PRICE CODE

17. SECURITY CLASSIFICATION OF REPORT	18. SECURITY CLASSIFICATION OF THIS PAGE	19. SECURITY CLASSIFICATION OF ABSTRACT	20. LIMITATION OF ABSTRACT
UNCLASSIFIED	UNCLASSIFIED	UNCLASSIFIED	

Acknowledgments

The author acknowledges technical assistance by Mr. Luis Ortega during the development of these instruments. Mr. Mike Rocha modified the tripod heads to provide azimuth and elevation readouts. Dr. Albert Forster of Forster Engineering Systems designed and built the VODDU units and made the hardware and software modifications to interface the Kodak still camera, azimuth-elevation read-outs, and GPS to the field computer.

Contents

Figures

Tables

1. Introduction

Interest in the effects of solid rocket motor (SRM) exhaust on the ozone concentration in the stratosphere led to the development of chemical and fluid dynamics models to predict local perturbation of the stratosphere by the plume. These models predict that stratospheric ozone levels in the plume will be depressed from ambient values by after-burning HCl,[1–5] which has been verified by recent in-situ measurements.[6] The size and persistence of the predicted reduced ozone concentrations are a sensitive function the plume dispersion rate. Previously, there were no imaging measurements of plume expansion as a function of altitude and launch conditions, and for longer than first 10 min after vehicle passage. Accordingly, some relatively inexpensive ground-based instruments were built to accomplish this task. This report describes the design and characteristics of these portable, field-grade instruments. The instruments were used for measurements of the dispersion rates of Titan IV and Space Shuttle SRM plumes at both the eastern and western test ranges. They can be used for other atmospheric studies, changing the observational band with a simple change of spectral filter if required.

The instruments electronically record images of a plume or contrail as it expands. The principal difficulty in accomplishing this task is the reduction of the contrast of the image in a bright sky as the plume becomes tenuous. These instruments enhance the contrast of the image of the plume using spectral filters and polarizers. This enhancement technique exploits the different spectral and polarization characteristics of sunlight that is Rayleigh-scattered from the troposphere and sunlight that is Mie-scattered from the plume in the stratosphere. This contrast enhancement permitted the observation time to be increased considerably beyond the 10 min previously attainable. Building several instruments permitted several altitudes to be observed simultaneously and observation of the plume from more than one location. Imaging the plume from at least two appropriately placed ground positions permits differentiation between plume expansion and plume shearing. This differentiation is important since expansion dilutes the chemical concentrations in the plume and changes the rate of the chemical reactions, whereas shearing may segment parcels of the plume without dilution.

2. Light Scattering Characteristics of the Atmosphere and Plume

2.1 Rayleigh Scattering from the Troposphere

The bright background against which the plume must be imaged is created principally by Rayleigh-scattered light from the air molecules in the troposphere. Rayleigh scattering theory is applicable to small, non-ionized, isotropic particles where the light is not near a resonance frequency of the particle, and the refractive index (m) of the particle is close to 1 (if m is appreciably greater than 1, then the condition $m\,x \ll 1$ where $x\ (=\pi D/\lambda)$ is the ratio of particle circumference to wavelength must be satisfied). For Rayleigh scattering theory to be valid, particles must have a radius r of 3% or less of the wavelength λ of the scattered light. Air molecules satisfy all these criteria except the requirement for isotropy, which causes a small deviation from the polarization characteristics of purely Rayleigh-scattered light (see Ref. 7). The cross section for Rayleigh scattering is[8]

$$\sigma(\theta) = \frac{16\pi^4 r^6}{\lambda^4}\left(\frac{m^2-1}{m^2+2}\right)^2 (1+\cos^2\theta), \tag{1}$$

where θ is the angle the scattered radiation makes with the forward direction. Two things should be noted in this expression: larger particles that meet the small-particle criterion scatter much more strongly than smaller particles; and short-wavelength radiation is much more strongly scattered than longer-wavelength radiation. Integrating this expression over all directions (requires replacing $(1+\cos^2\theta)$ by $8\pi/3$) and dividing by the geometric cross section yields the scattering efficiency. Noting that the scattering cross section and radius for N_2 are approximately 4×10^{-28} cm^2 at 1.0 μm and 1.75×10^{-8} cm, respectively,[7] we find the scattering efficiency to be about 4×10^{-13}. This can be compared with Mie scattering efficiencies given below for the plume particles that can be greater than 1.

Because the particle is small compared to the wavelength of the scattering radiation, the electric field is constant over the particle and thus induces an oscillating dipole moment that leads to classical dipole radiation and polarization patterns. These patterns are shown in Figure 1 for isotropic scattering centers. The polarization is

$$P \equiv \frac{I_s - I_p}{I_s + I_p} = \frac{1-\cos^2\theta}{1+\cos^2\theta}, \tag{2}$$

where I_s (I_p) is the intensity of scattered radiation with polarization perpendicular (parallel) to the scattering plane. The scattering plane is defined as the plane that contains the radiation source (sun), the scattering center (the position in the plume imaged), and the observation point (camera). Thus, for pure Rayleigh scattering, the radiation is unpolarized along the scattering direction (0° in Figure

1) and 100% polarized perpendicular to the scattering plane in a direction perpendicular to the scattering direction (90° in Figure 1).

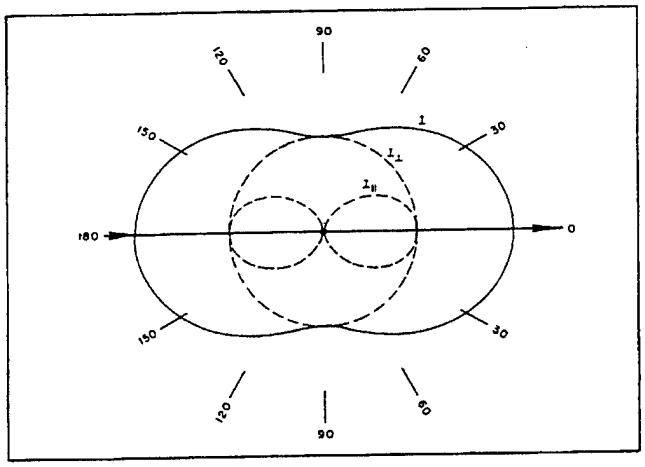

Figure 1. Spatial Distribution of polarized Rayleigh-scattered radiation.

According to the above, if the atmosphere were a perfect Rayleigh scattering medium, the sky would be 100% polarized in directions perpendicular to the line between the plume section imaged and the sun. There are four phenomena that reduce this degree of polarization:[7] (1) the anisotropy of the air molecules mentioned above; (2) multiple scattering; (3) turbidity (aerosol content) of the atmosphere; and (4) the albedo or reflectivity of the Earth's surface. The anisotropy leads to a depolarization of about 1%; multiple scattering increases with decreasing wavelength according to Eq. (1) and can reduce the polarization by up to 50% at high optical thickness in directions of about 100° from the sun in the plane of the sun's vertical. The albedo (high over snow-covered ground) and the turbidity (high in hazy weather) can reduce the polarization by 20–40 % at their most effective sun angles. The depolarizations by these environmental effects were much less than these maximum values for the conditions encountered during the plume observations.

2.2 Mie Scattering from the Stratosphere

Mie scattering calculations will accurately predict the characteristics of the scattered radiation for any particle size with any index of refraction. These calculations require knowledge of the particles in the plume, including their shape, refractive index, composition, size distribution, and density. Recently, a study was completed that presented this particle information and developed a model of the plume of SRM exhaust for the size-specific particle density in the stratosphere.[9] Mie scattering calculations were also completed that predict the characteristics of the scattered radiation for the particle size distribution given by this particle model.[10] We draw on information from these two publications to aid in the instrument design.

* Some recent LIDAR backscattering measurements from a section of a stratosphere SRM plume have shown a λ^{-4} dependence in the visible and UV spectral region.[11] This is consistent with small-particle (Rayleigh) scattering.

The particles are liquid when ejected from the rocket and condense within a few seconds to solid spheres of primarily Al_2O_3. The particle size distribution is tri-modal with average particle sizes (Sauter mean diameters) of 0.056, 1.0, and 3.6 μm. The model of particles in the plume allows the particle number density as a function of particle size to be calculated for expansion times after the rocket passage at altitudes between 18 and 40 km. Results from this model are shown in Table 1 for a Titan IV rocket 10 min after vehicle passage.

From this table, we see that the small-particle mode has a number density 3 orders of magnitude greater than either the medium- or large-particle modes. We also note that much of the scattering from this small-particle mode could be predicted using Rayleigh scattering theory (but is more accurately predicted by Mie theory). Even though the small-size particle has the advantage of having a greater number density, they scatter very little light, as can be seen in Table 2. In this table, the scattering efficiencies $\overline{Q}$ and attenuation β_{avg} due to Mie scattering are given for four wavelengths for the three particle modes. Note that the scattering efficiencies are above 1.0 for the medium- and large-particle modes and 10^{-6} or less for infrared wavelengths for the small particles. The Mie scattering attenuation coefficient (defined by the relation $I / I_0 = \exp(-\beta_{avg} l)$ where l is the path length) increases with wavelength and is 2 to 3 orders of magnitude greater for the large-particle mode than the medium-particle mode at infrared wavelengths. Thus, nearly all the light scattering is caused by the large-particle mode, which scatters the infrared wavelengths more efficiently than the visible wavelengths.

The polarization characteristics of Mie scattering for a $x = 3$ ($D \cong \lambda$) are shown in Figure 2 for a non absorbing particle with a real refractive index of 1.315. These curves show that the radiation is polarized parallel to the scattering plane at scattering angles between 90° and 150° with the polarization peaking near 120°. Thus in this angular range, the light scattered from the particles is polarized perpendicular to the light scattered from the air in the troposphere.

Table 1. Plume-Particle Characteristics at 10 min of Expansion[9]

Particle Mode	Sauter Mean Diameter D_{32} (μm)	Mass Fraction in Particle Model	C_m Mass per Volume Air: Peak Value (gm/cm^3)	Number Density: Peak Value (cm^{-3})
Small	0.056	0.012	2.0×10^{-12}	8.8×10^3
Medium	1.0	0.015	2.4×10^{-12}	7.94
Large	3.6	0.974	1.6×10^{-10}	6.16

Table 2. Particle Scattering Efficiencies and Attenuation Coefficients[10]

Mode	D_{32} (μm)	$\lambda = 0.2$ μm		$\lambda = 0.5$ μm		$\lambda = 1.0$ μm		$\lambda = 5.0$ μm	
		$\overline{Q}$	β_{avg}(cm^{-1})	$\overline{Q}$	β_{avg}(cm^{-1})	$\overline{Q}$	β_{avg}(cm^{-1})	$\overline{Q}$	β_{avg}(cm^{-1})
Small	0.056	0.57	1.1E-6	0.015	3.0E-8	1.6E-5	3.2E-11	1.5E-6	3.0E-12
Medium	1.0	2.35	3.7E-7	2.74	4.3E-7	0.9	1.4E-7	0.13	2.0E-8
Large	3.6	2.15	8.6E-6	2.3	9.2E-6	2.9	1.2E-5	3.3	1.3E-5

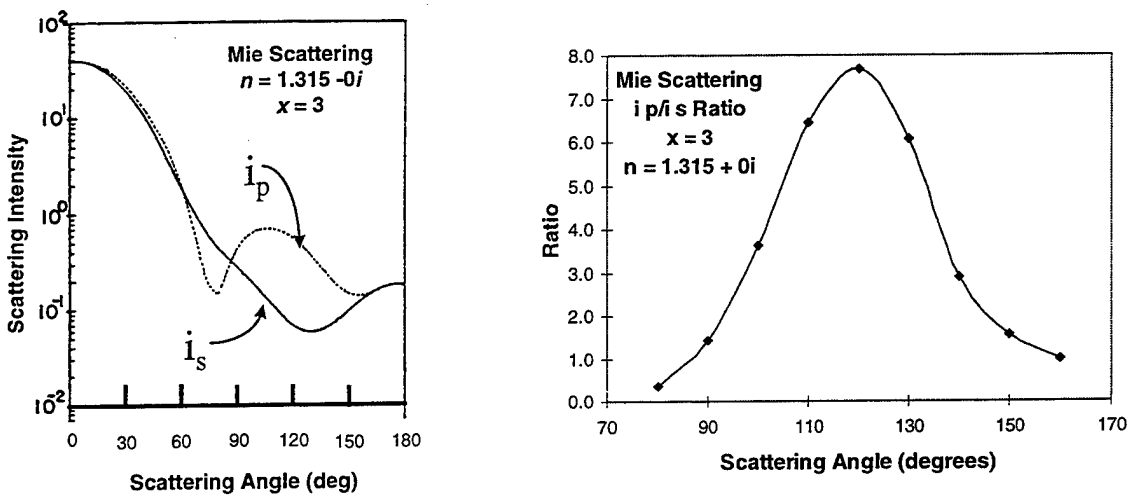

Figure 2. Characteristics of Mie scattered radiation.[8]

3. Design and Characteristics of the Instruments

The discussion above suggests that an effective strategy to increase the contrast of the plume against the Rayleigh background from the troposphere is: (1) view the plume at the longest wavelengths possible thus reducing the intensity of the Rayleigh-scattered radiation from the troposphere though the $1/\lambda^4$ factor in Eq. (1) and reducing the depolarization caused by multiple scattering; and (2) view the plume at a 90° scattering angle with a polarizer orientated to view light scattered parallel to the scattering plane. This strategy maximizes the signal scattered from the plume since the Mie scattering is greatest at longer wavelengths and polarized predominately in the plane parallel to the scattering plane, and discriminates against the perpendicularly polarized Rayleigh-scattered light from the troposphere.

The longest wavelength that can be used is dictated by spectral sensitivity of the camera, assuming that there is adequate radiation available from the sun at the chosen wavelength. The camera is a silicon-based CCD that is sensitive to radiation at wavelengths of less than 1.1 μm with a peak sensitivity near 0.8μm (see Appendices I and II). The sun's spectral peak is near 500 nm and drops to about half of its stratospheric value at 1.0 μm (see Appendix IV). The intensity at wavelengths on either side of 1.0 μm is reduced by another factor of 2 in the troposphere by water absorption bands. Thus, the spectral region near 1.0 μm appears to be a practical band in which to record scattered sunlight from the plume from the ground.

The effectiveness of this strategy depends on the relative positions of the sun, plume, and camera and the atmospheric conditions at the time of launch. To see if these conditions can be met for a given launch window and available observation position, we must consider the scattering geometry in terms of the latitude and longitude of the observation point and the vehicle trajectory as well as the azimuth and elevation of the sun. This is done in the next section.

3.1 Scattering Geometry

The scattering geometry is shown in Figure 3. The scattering plane is defined by the sun, the scattering point in the plume, and the observation point (O). The scattering angle θ_{scat} is defined as the angle between the forward direction of the incident radiation from the sun and the scattered radiation into the camera. The polar coordinates are designed by r, θ, ϕ. Given the azimuth and elevation angles for the plume and sun, their polar coordinates can be found using:

$$\begin{aligned} \phi &= 180^o - az; \quad az = 0^o \text{ to } 180^o \\ \phi &= 540^o - az; \quad az = 180^o \text{ to } 360^o \\ \theta &= 90^o - el; \quad el = 0^o \text{ to } 90^o \end{aligned} \tag{3}$$

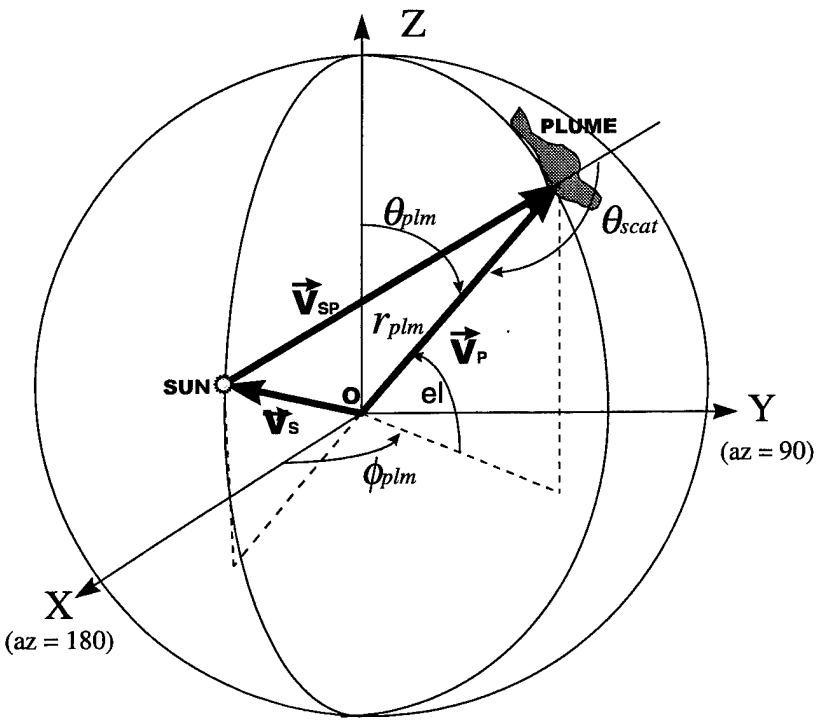

Figure 3. The scattering geometry showing the definition of the scattering angle. The three vectors lie in the scattering plane. The polarization of the scattered light is defined with respect to this plane.

By defining vectors from the observation point (origin) to the sun and plume scattering point, we note that the scattering angle is given by

$$\theta_{scat} = 180^o - \cos^{-1}\left(\frac{\vec{v}_{sp} \cdot \vec{v}_p}{|\vec{v}_{sp}||\vec{v}_p|}\right) \tag{4}$$

where

$$\vec{v}_{sp} = \vec{v}_p - \vec{v}_s \tag{4}$$

and the position vectors of the sun and plume in terms of spherical coordinates are, respectively,

$$\begin{aligned} \vec{v}_s &= r_s \sin\theta_s \cos\phi_s \hat{i} + r_s \sin\theta_s \sin\phi_s \hat{j} + r_s \cos\theta_s \hat{k} \\ \vec{v}_p &= r_p \sin\theta_p \cos\phi_p \hat{i} + r_p \sin\theta_p \sin\phi_p \hat{j} + r_p \cos\theta_p \hat{k} \end{aligned} \tag{6}$$

Thus, the scattering angle is

$$\theta_{scat} = 180^o - \cos^{-1}\left(\sin\theta_s \cos\phi_s \sin\theta_p \cos\phi_p + \sin\theta_s \sin\phi_s \sin\theta_p \sin\phi_p + \cos\theta_s \cos\theta_p\right) \quad (7)$$

Using Eqs. (3) in Eq. (7) allows the scattering angle to be calculated given the azimuth and elevation of the sun and (from the trajectory of the vehicle and the latitude and longitude of the observation site) latitude and longitude of the initial plume scattering point. Using a pre-calculated trajectory to obtain the vehicle position and a FORTRAN subroutine based on data from the Astronomical Almanac (U.S. Government Printing Office, Washington, D.C., 1985) to calculate the sun azimuth and elevation, this calculation was performed before each launch for all plumes studied. An example of the results of this calculation is shown in Figure 4 for the trajectory of the Space Shuttle flight launched 7 August 1997 (STS-85) from KSC viewed from Haulover Canal, a site north of the launch pad. The results are shown as a function of vehicle altitude for a time period that encompasses the launch window. For this observation point, all the criteria for this contrast-enhancing technique are met throughout in the launch window for stratospheric altitudes. This calculation gives the scattering angle for the initial position of the plume. As the plume expands and blows across the sky, these conditions will change in ways that are only partially predictable.

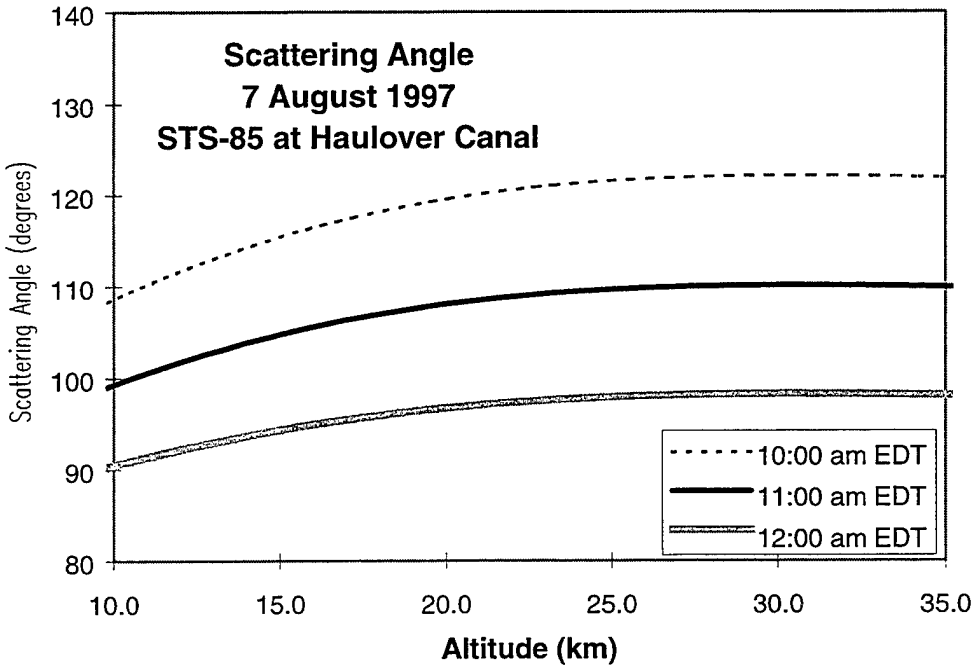

Figure 4. Predicted scattering angle for STS-85 flight from Haulover Canal site at Cape Canaveral. Launch occurred at 10:41 a.m. EDT.

3.2 Video Instruments Description

With these considerations in mind, three CCDTV-video tape instruments and one high-resolution electronic still camera instrument were built. Figure 5 shows the principal components of the video instruments. The camera for this instrument is a Hitachi KP-160 high-sensitivity CCD with 786 horizontal and 488 vertical pixels. The pixels have a 100% fill factor. With the IR cut-off filter removed, the spectral sensitivity peaks at 800 nm and has good response to 1100 nm. The filter and polarizer were cut to fit in standard 49-mm-diam camera threaded lens mounting rings. This allowed quick interchange and stacking of optical components. The camera was equipped with an 8–48 mm zoom lens, a spectral filter, and IR polarizer. The spectral response curves for the camera, filter, and polarizers are presented in Appendix I. The composite spectral response curves for the instruments are shown in Figure 6 and have a peak near 900 nm. The two different curves are due to the two different polarizers that are used on different cameras.

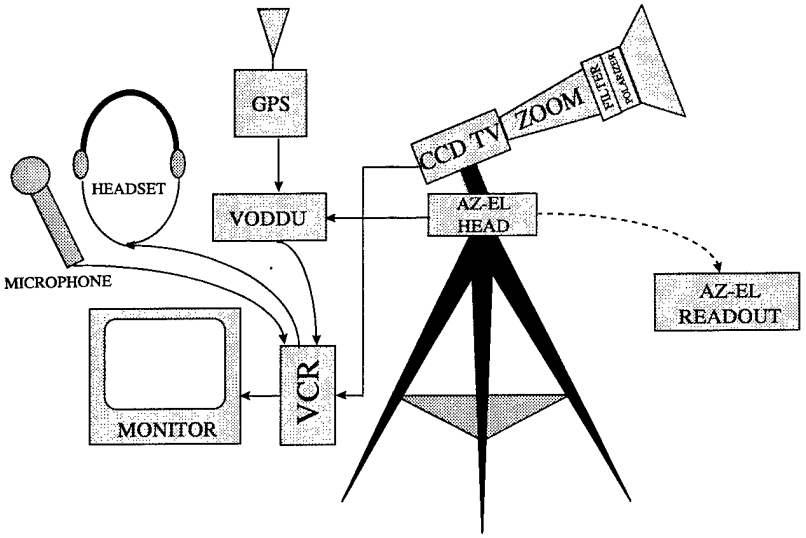

Figure 5. Video instrument configuration.

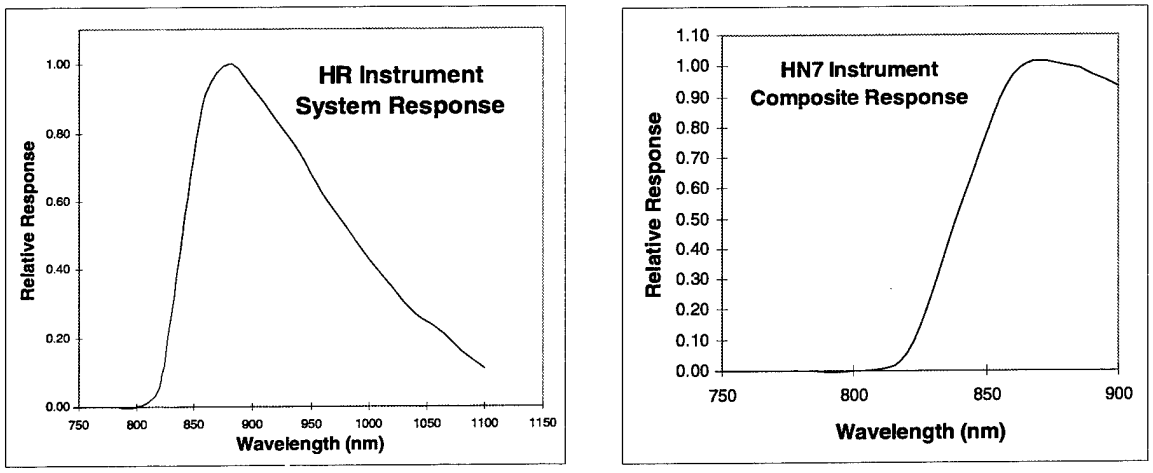

Figure 6. Spectral response of video instruments when configured with HR (left) and HN7 (right) polarizers.

The video images are recorded at SVHS resolution with voice annotation using portable video recorders. The cameras are mounted on commercial tripod heads that were modified with two pairs of orthogonally mounted gears, each pair coupled to an optical encoder that feeds signals to digital readouts for the azimuth and elevation of the imaging direction. At the end of the plume measurement program, the encoder outputs were fed to a custom-built video overlay data display unit (VODDU) that recorded the azimuth and elevation, latitude, longitude, and universal time (from a GPS) on a raster strip at the bottom of the screen. The images are monitored in real time using small high-resolution black and white video monitors. All equipment is installed on a folding shelf supported by the tripod. The equipment for each instrument, with the exception of the tripod, is transported in a compact 12" x 18" x 30" plastic case that can be checked as airline luggage.

The fields-of-view (FOV) of the systems as a function of lens focal length are shown in Figure 7. Details on the measurement and spatial calibration of the instruments are given in Appendix III. The half-inch c-mount format of the camera permits an extremely wide range of focal lengths and hence a wide range of fields-of-view to be realized in a relatively inexpensive lens. A sun shield was installed in front of the polarizer, which is often required at the short focal lengths. This wide range of fields-of-view enables images with good spatial resolution to be recorded of the plume for nearly an hour of expansion. The azimuth and elevation readouts allow the change in the plume centerline to be recorded from which the wind direction and speed can be inferred by using the assumption that there is no vertical component to the stratospheric winds.

3.3 Electronic Camera Instrument Description

Due to raster noise, the signal-to-noise ratio of images taken from video signals is seldom greater than 5 bits (32 gray levels). In order to enhance the spatial resolution contrast through image processing, a Kodak Megapixel 1.6i CCD camera was acquired. This camera has 1.533 million pixels, each with 10-bit intensity resolution (1024 gray levels). This camera was mated to a spectral filter and polarizer and controlled with a fast digital frame grabber installed in a PCI bus Pentium computer (see Figure 8). The composite spectral response of the instrument is present in Figure 9.

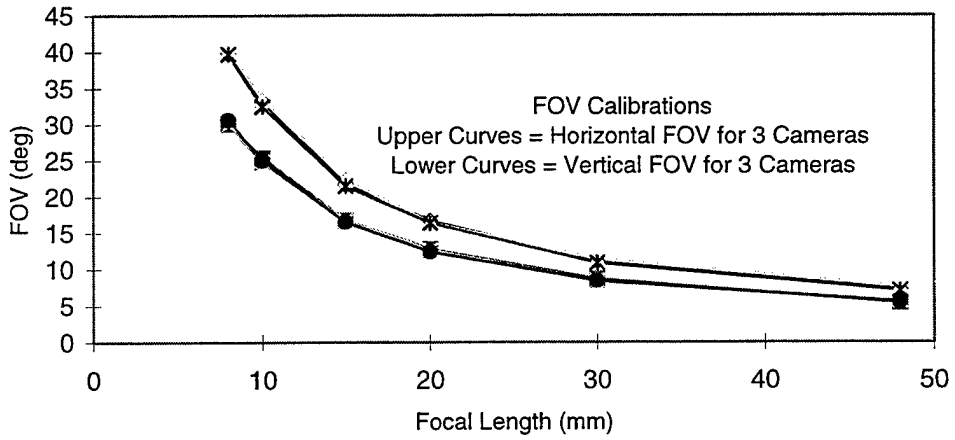

Figure 7. Field-of-view of video instruments using the 8–48 mm zocm lenses.

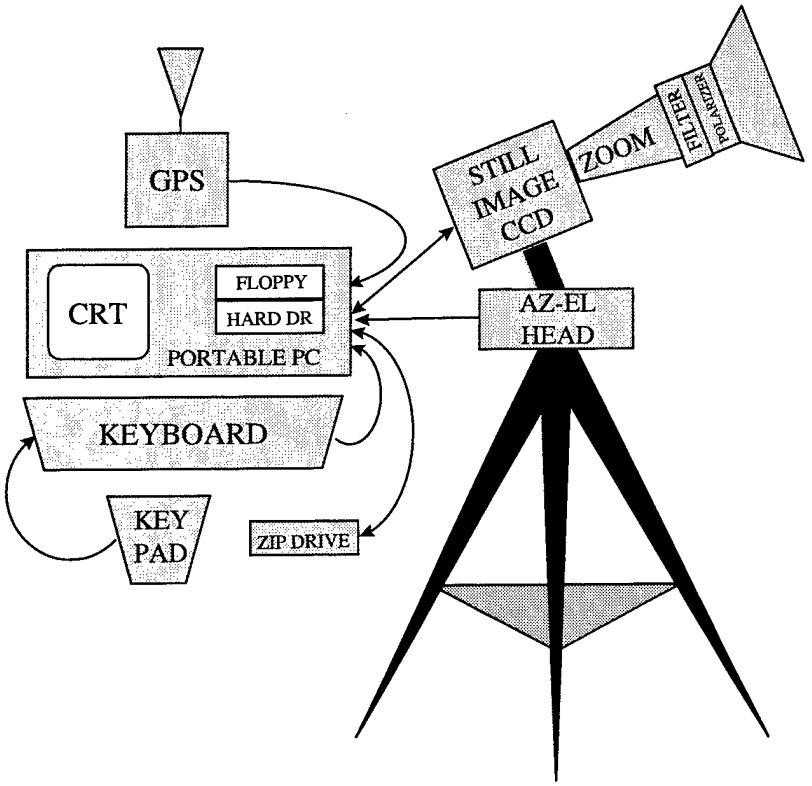

Figure 8. Configuration of still image electronic camera system.

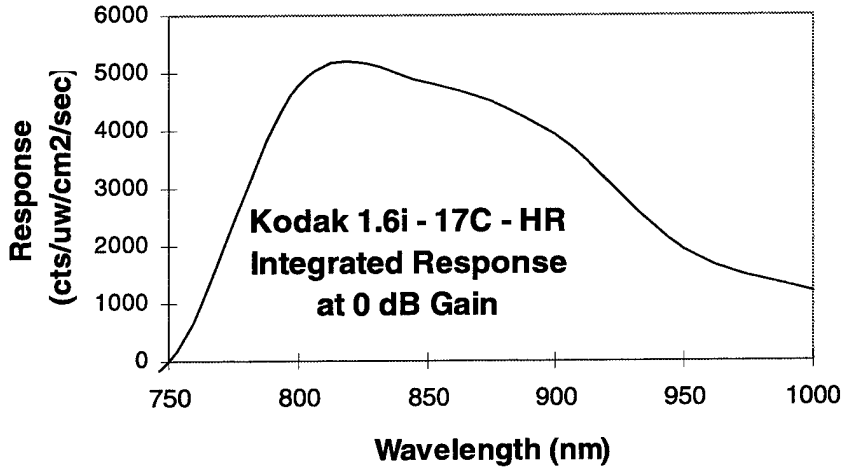

Figure 9. Spectral response of still imaging system comprising the Kodak Megapixel 1.6I camera, Kodak Wratten 87C filter, and Polaroid HN polarizer.

This instrument was equipped with a standard 35-mm (F-mount) wide-angle zoom lens. The filter and polarizer for this instrument had to have a much greater diameter (82 mm) than required for the c-mount lenses (49 mm). A sun shade was also required for this system. The results of the field-of-view measurements are presented in Table 3 (see Appendix III for details). These measurements were taken for only the two extreme focal lengths of the zoom lens. Equipped with this lens, this instrument has nearly the same maximum FOV as the video instruments but has a much greater spatial and contrast resolution. The camera has 1500 pixels in the horizontal directions and 1022 pixels in the vertical direction. The T+ time is continuously displayed on the computer monitor (set to zero by pressing the F1 key at T = 0). During measurements, the camera continuously takes exposures and displays them on the monitor. Pressing the space bar of the keyboard (or a button on a shutter custom box) recorded the image on hard drive with the T+ time as the filename.

For the last two observations (STS-90 and STS-91), a custom ISA board was added to the computer that reads the encoder pulses from the tripod and displays the azimuth and elevation on the monitor in real time. Additionally, a GPS receiver was also added, and custom hardware and software added the latitude, longitude, and universal time to the screen. These screen displays as well as the T+ time were recorded in the first 100 bytes of the image file. A list of the characteristics of the components are presented in Appendix II.

Table 3. Still Imaging System Field-of-View

Focal Length (mm)	Horizontal FOV (deg)	Vertical FOV (deg)	Angular Dispersion (deg/pixel)
18	40.6	27.6	2.73×10^{-2}
35	23.0	15.6	1.525×10^{-2}

4. Performance

The video instruments were used to record the plume expansion of seven launches: shuttle launches STS-80, -83, -94, -85, -90, -91 from CCAS, and Titan IV launch K-13 from VAFB. The Titan IV launch was notable because the plume expansion was recorded from two locations simultaneously: a land location on an unimproved location on Bixby Ranch and from the helicopter platform on a oil platform located 10 km offshore. In all cases, the video instruments performed flawlessly. Under all conditions, the images recorded by the cameras clearly have more contrast than the plume viewed by eye. The largest part of this increase in contrast was due to viewing the plume in the infrared. When the scattering angle was between 90° and 120°, rotating the polarizer parallel to the scattering plane did perceptibly increase the visibility of a tenuous plume; the magnitude of increased visibility was dependent on the atmospheric conditions An example of a frame from the video recording of the K-13 launch is given in Figure 10. The center of this frame shows the plume at T+ 4:00 minutes at an altitude of 30 km. The measurement of the plume diameters are not taken from poor-quality frame-grabbed hardcopies such as that given in Figure 10, but from a large (41.4 x 30.8 cm) video monitor where the eye temporally integrates many frames, giving a much clearer, higher-contrast view of the plume.

The still imaging instrument was available only for the last four STS observations and performed well on three of these four outings—experiencing data loss on one due to software problems. Its images have better contrast and spatial resolution than those of the video. An example of a digitally un-enhanced image from this instrument is shown in Figure 11. The clarity of the plume section of interest can be improved significantly by numerical algorithms that compress the information from the 10-bit gray scale available electronically to the much more limited gray scale available in a laser printer image. Here the plume of STS-83 is shown at T+ 233 seconds where the positions of 24 km and 30 km altitudes are indicated. The bright plume on the left side of the image is the tropospheric portion of the plume that is blowing in front of the (stationary) stratospheric section of the plume. Unfortunately, it was obscuring of the stratospheric portion of the plume by clouds or a tropospheric plume segment and not a lack of contrast that limited the observing time during most launches using these instruments.

If the view of the plume was unobstructed, observations could be make up to an hour. The longest expansion time recorded (50 min) was terminated by the edge of the plume expanding beyond the field-of-view of the camera when its lens was set at its shortest focal length. Thus, these instruments increased the contrast of the tenuous plume sufficiently so it was no longer the limiting factor to long duration of plume expansion measurements.

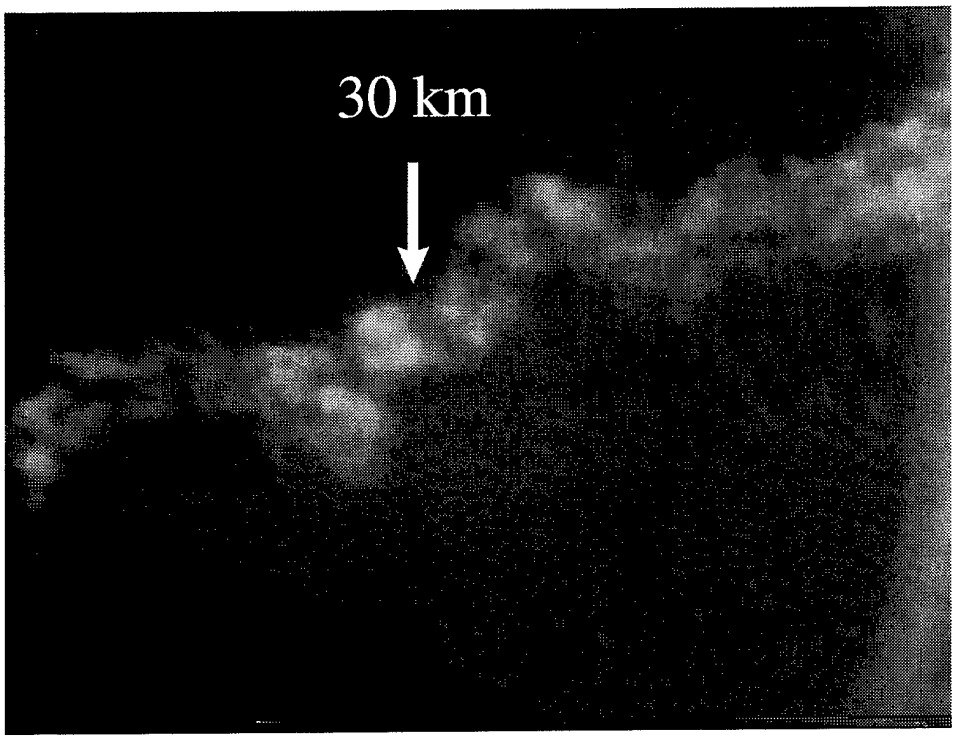

Figure 10. Frame from video instrument showing view of K-13 plume at T+ 240 seconds. This images was recorded at Bixby Ranch. The plume at an altitude of 30 km is indicated.

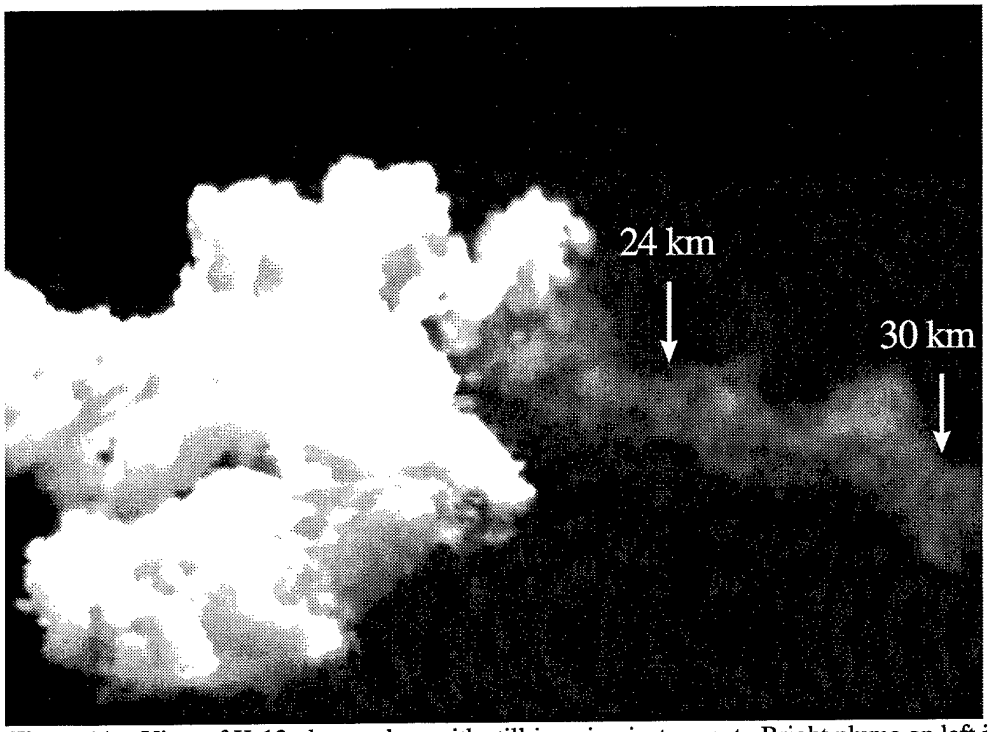

Figure 11. View of K-13 plume taken with still-imaging instrument. Bright plume on left is tropospheric plume blowing into field of dimmer stratospheric plume on right.

5. Summary

The techniques and instruments described in this report served to create a database that will be used to predict the effects of SRM exhaust on the stratosphere. The combination of long-wavelength observation, polarization selection, image processing, and wide-angle zoom lenses allowed the plume expansion to be observed for to up to 50 min, 5 times the longest previous measurements. These very portable instrument are useful for other atmospheric measurements (both particle and chemical), their versatility being extended through easy changes in their lenses, filters, and polarizers.

References and Notes

1. Kruger, B.C., "Ozone Depletion in the Plume of a Solid-fuel Rocket," *Ann. Geophysicae* Vol. 12 No. 5, 1994, pp. 409-416.

2. Denison, M.R., Lamb, J. J., Bjorndahl, W.D., Wong, E.Y., and Lohn, P.D., "Solid Rocket Exhaust in the Stratosphere: Plume Diffusion and Chemical Reactions," *J. Spacecraft & Rockets* Vol. 31 No. 3, 1994, pp.435-442.

3. Brady, B.B., and Martin, L.R., "Modeling Solid Rocket Booster Exhaust Plumes in the Stratosphere with SURFACE CHEMKIN," The Aerospace Corp., TR-95(5231)-9, El Segundo, CA, Sept. 1995.

4. Zittel, P.F., "Computer Model Predictions of the Local Effects of Large, Solid-fuel Rocket Motors on Stratospheric Ozone," The Aerospace Corp. TR-94(4231)-9, El Segundo, CA, Sept. 1994.

5. Ross, M., "Local Impact of Large Solid Rocket Motor Exhaust on the Stratospheric Ozone and Surface Ultraviolet Flux," *J. Spacecraft & Rockets* Vol. 33 No. 1, 1996, pp. 144-153.

6. Ross, M. N., Benbrook, J. R., Sheldon, W. R., Zittel, P. F., and McKenzie, D. L., "Observation of Stratospheric Ozone Depletion in RocketPlumes, *Nature* **390**, 62-65, 1997.

7. If the refractive index m and the number density of molecules n are known, the total scattering cross section can be accurately calculated from

$$\sigma(\lambda) = \frac{24\pi^3}{n^2\lambda^4}\left(\frac{m^2-1}{m^2+2}\right)^2 \frac{6+3\Delta}{6-7\Delta}$$

where the depolarization Δ compensates for anisotropic scatterers and is defined as the ratio of the two polarized intensities at a 90° scattering angle ($\cong 0.028$ for dye air). Multiplying this expression by the phase function $P(\theta)$ gives the differential cross section:

$$P(\theta) = \frac{3}{16\pi}\frac{2}{(2-\Delta)}\left[(1+\Delta)+(1-\Delta)\cos^2\theta\right]$$

Neglecting the depolarization and assuming m is near 1, the expression for the total cross section is simplified to

$$\sigma(\lambda) = \frac{32\pi^3}{3n^2\lambda^4}(m-1)^2$$

The Rayleigh total cross section of air is 4.0 x 10^{-28} cm^2 at 1.0 μm. [Handbook of Geophysics and the Space Environment, A. S. Jursa, Ed., Air Force Geophysics Laboratory, 1985, pp. 18-7 - 18.9.]

8. Coulson,, K. L, *Polarization and Intensity of Light in the Atmosphere*, A. Deepak Publishing, Hampton, Virginia, USA, 1988.

9. Beiting, E. J., "Solid rocket Motor Exhaust Model for Alumina Particles in the Stratosphere," *J. Spacecraft and Rockets*, **34** No. 3, May-June, 1997, pp. 303-310.

10. Beiting, E. J., "Predicted Optical Characteristics of Solid Rocket Motor Exhaust Model in the Stratosphere," *J. Spacecraft and Rockets*, **34** No. 3, May-June, 1997, pp. 311-317.

11. Dao, P. D., Gelbwachs, J., Farley, R., Garner, R., and Soletsky, P., "LIDAR Stratospheric SRM Exhaust Plume Measurements, 35th AIAA Aerospace Sciences Meeting, Reno, NV, paper AIAA-97-0526.

10. Forster Systems Engineering, 35 Chicory Way, Irvine, CA 92715. 714-733-07678

11. Tangent Instruments, Inc. 1691 Spinnaker Drive, Suite 202, Ventura, CA 93001

Appendix I—Video Instruments' Components and Specifications

Information and specifications of the components used in the near IR video recording instrument are presented in this appendix. The list of components and characteristics are given in Table I-1. The spectral responses of the camera, filter, and polarizers are presented in Figure I-1. The extinction characteristics of the polarizers are presented in Figure I-2 . The extinction ratio is defined as the ratio of the maximum transmitted intensity to the minimum transmitted intensity when the polarizer is illuminated with 100% polarized radiation. The spectral characteristics of the HN7 polarizer were not available beyond 900 nm. The HN7 polarizers are considerably less expensive than the HR polarizers.

Table I-1 Near-IR Video Recording Instrument Components

Component	Manufacturer	Model	Characteristics
Camera	Hatachi	KP-160	B/W High Sensitivity Near IR
Zoom Lens	Computar	H6Z0812	8-48 mm, F/1.2-16C
Filter	Melles Griot	03 FCG 118	RG850 IR Black Glass
Polarizer	Polaroid	HR and HN7	IR Sheet Polarizer
Video Recorder	Panasonic	AC-CR20P	SVHS Portable
Monitor	Ultrak	UL-KM-9	9" B/W High Resolution
Az-El Readout	Tangent Instr. Inc [11]	ASP3 Version 0.97	Expects 2048 pulses/rev
Tripod	Bogen	3231	3126 Fluid Head
Tripod Gear	PIC Design	AB21-72	72 tooth
Tripod Gear	PIC Design	AB19-120	120 tooth
Tripod Encoders	Tangent Instr. Inc [11]	E2160	2160 pulses/rev

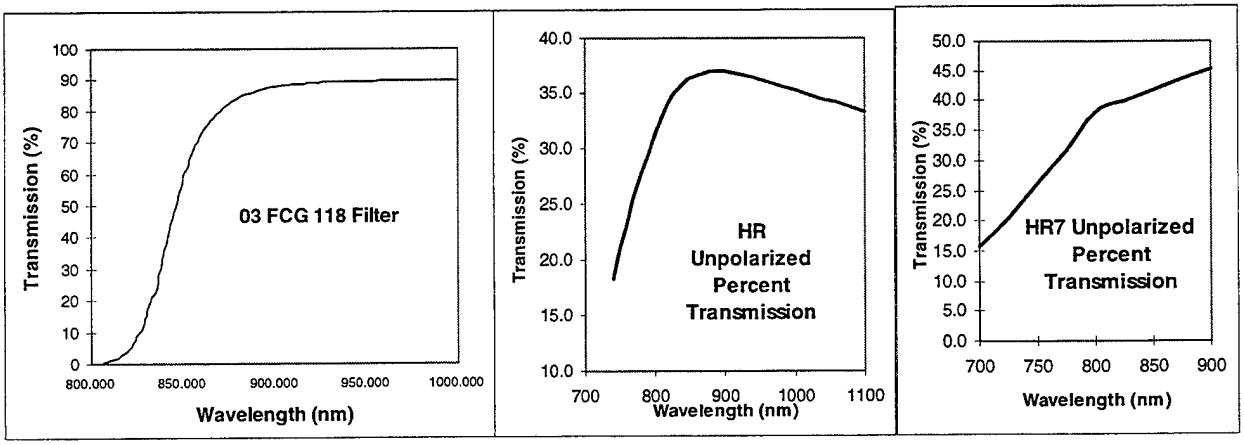

Figure I-1. Spectral responses of filter and polarizers.

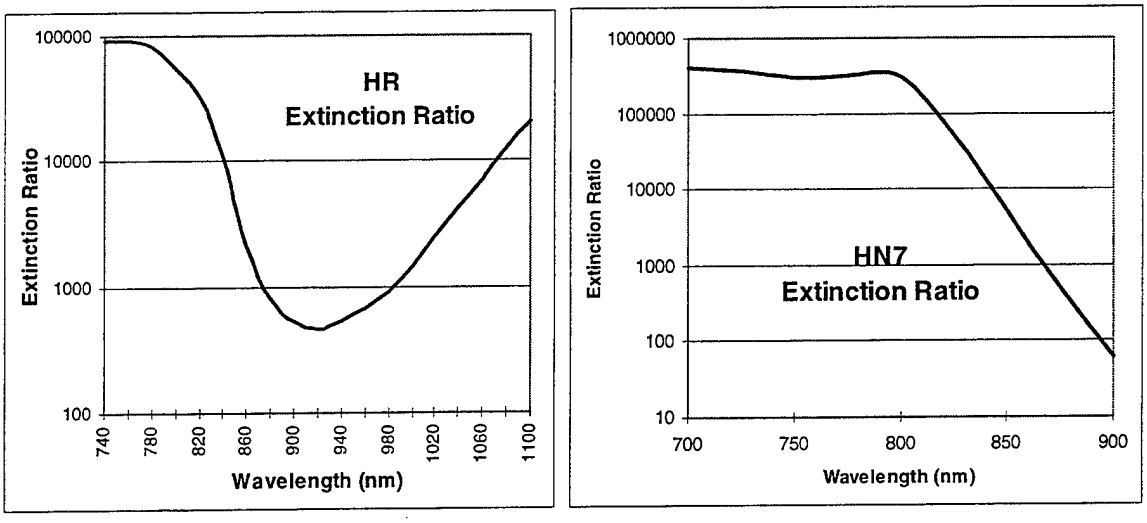

Figure I-2. The extinction ratio curves of the two polarizers used on the video instruments. The extinction ratio is defined as the ratio of the maximum transmitted intensity to the minimum transmitted intensity when the polarizer is illuminated with 100% polarized radiation.

The custom modifications to the tripod allowed the azimuth and elevation to be digitally displayed on a readout box. The box expects an encoder that produces 2048 pulses/360° but allow a scaling factor to be input to correct for other encoders. The box does not allow additive constants to be inserted so the displayed box must always be zeroed with the camera pointed due north and level. The scaling factor is calculated from:

= (2048 box expected encoder)/(2160 actual encoder) x (72 gear teeth @ encoder)/(120 teeth @ driver) = -0.5689 on channel 1

This display box was later replaced by the VODDU that allowed for arbitrary direction initialization and automatically recorded azimuth, elevation, latitude, longitude, and universal time on the video tape.

Appendix II—Still Camera Instrument Components and Specifications

Information and specifications of the components used in the near-IR high-resolution still instrument are presented in this appendix. The list of components and characteristics are given in Table II-1. The spectral response and gain characteristics of the camera are presented in Figure II-1. The spectral response of the 87C Wratten filter are presented in Figure II-2. The spectral response and extinction characteristics of the HR polarizer are presented in Figures I-1 and I-2.

Table II-1. Near-IR Still Imaging Instrument Components

Component	Manufacturer	Model	Characteristics
Camera	Kodak	Megapixel 1.6i	1.533 x 10^6 pixel; 10 bit
Zoom Lens	Sigma	Aspheric Zoom	18-35 mm, F/3.5-22; 82 mm
Filter	Kodak	Wratten 87C	Visible Blocking, Gel Filter
Polarizer	Polaroid	HN7	IR Sheet Polarizer
Image Capture Board	Imaging Technology	IC-PCI-410-KIT-P	
Computer	Broadax Systems, Inc.	P5-120-PCI/32 MB	Built-in 9.5" Color Monitor
GPS	Forster Systems Eng[12]		Custom on Stand GPS Board
Internal Az-El	Forster Systems Eng[12]	Custom	ISA Board
Tripod	Bogen	3231	3126 Fluid Head
Tripod Gears	PIC	J24-80	80 Tooth Hubless Al Gear
Tripod Gears	PIC	P14-4-40	40 Pitch Anti-Backlash Gear
Tripod Encoders	Tangent Instr. Inc[13]	E2160	2160 pulses/rev

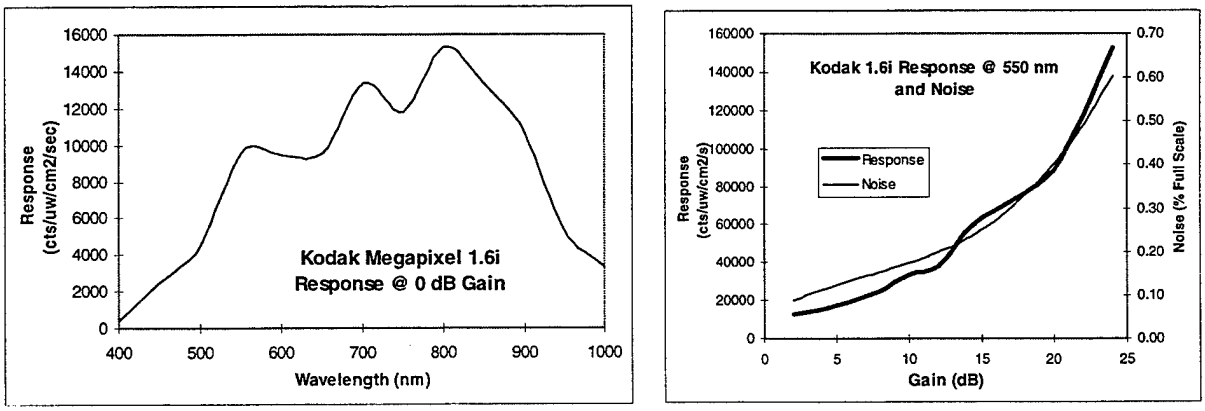

Figure II-1. Characteristic of the Kodak Megapixel 1.6i CCD camera. The spectral response is presented on the left plot for 0 dB gain. The sensitivity and noise characteristics as a function of gain are presented in the right plot. The equivalent photographic speed ratings (ISO) vary between 100 (0 dB) and 1500 (24 dB).

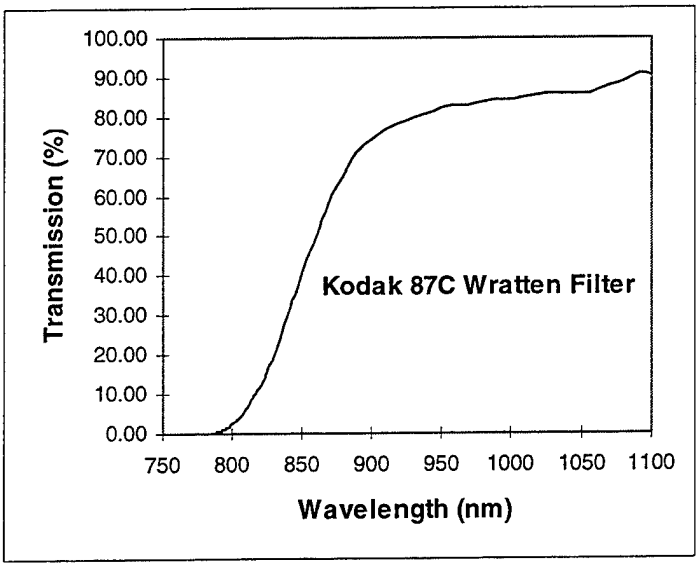

Figure II-2. Spectral transmission of Kodak 87C Wratten Filter

The azimuth-elevation was read out, displayed on the computer screen, and recorded in the image file (replacing the first 100 bytes of pixel information) by custom hardware and software to about 0.1° accuracy. Two values must be place in the computer for proper values: a scale factor that depends on the gears and encoder and an initial constant that allow the system to be zeroed at an arbitrary azimuth and elevations. The display output is calculated from:

The display output = factor * encoder value + initial constant.

factor =360 deg/(gear ratio*2160 encoder pulses per rev)

= 360/((120/72)*2160) = 0.1 for nylon gears

=360/((80/40)*2160) = 0.08 for metal anti-backlash gears

Appendix III—Instrument Spatial Calibration

The transverse extent of the plume was inferred from the size of this image on the playback monitor (for the video instruments) or hardcopy (for the still electronic camera) using the calibration method described here. Referring to Figure III-1, the physical feature of extent L at distance R from the camera with an angular extent θ is imaged by a lens onto the CCD surface, creating an image that is transferred to the readout surface with an extent l at an effective distance r with the same angular extent In the field, we wish to infer L from a measured l and known R using the relation: $L/R = L/r$. In the laboratory, we measure l for a known L at a known R to obtain r. The value of r will be different for different readout devices and different focal lengths of the lens. For the Kodak still-image camera, the readout was a laser printer image of dimensions 20.3 x 13.8 cm. For the video cameras, the readout was a Proscan SVHS monitor of dimensions of 41.4 x 30.8 cm. In the laboratory, $L = 1$ m and $R = 15.24$ m (50 ft). The results are given in Table III-1.

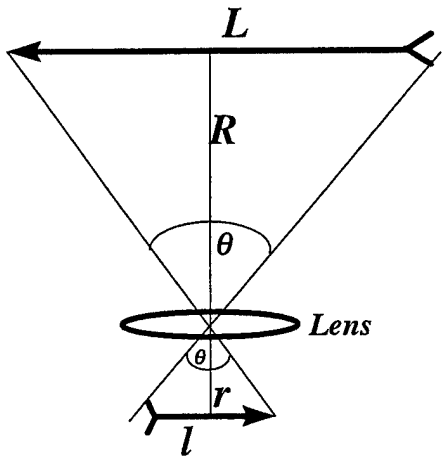

Figure III-1. Lens imaging geometry used for calibration.

Table III-1. Camera Calibration Parameters

Camera	Focal Length (mm)	Lab *l* (cm)	*r* (cm)	Dispersion (deg/cm)	V FOV (deg)	H FOV (deg)
Kodak Still	18	1.8	27.43	2.09	27.6	40.6
Kodak Still	35	3.275	49.91	1.15	15.6	23.0
Video	8	3.85	58.67	0.940	28.9	38.9
Video	10	4.5	68.58	0.812	25.0	33.6
Video	15	6.9	105.2	0.539	16.6	22.3
Video	20	9.0	137.2	0.414	12.8	17.2
Video	30	13.6	207.3	0.275	8.48	11.4
Video	45	21.9	333.8	0.171	5.28	7.10

Appendix IV—Solar Spectrum

The light available for scattering and detection is determined from the solar spectrum in the stratosphere and troposphere, respectively. The solar spectrum is presented in Figure IV-1. This figure indicates that 50–70% of the radiation on the short-and long-wavelength side of the 1.0 μm spectral region is absorbed by water in the troposphere. The solar spectrum is greatly attenuated in the visible and ultraviolet spectral regions by stratospheric ozone.

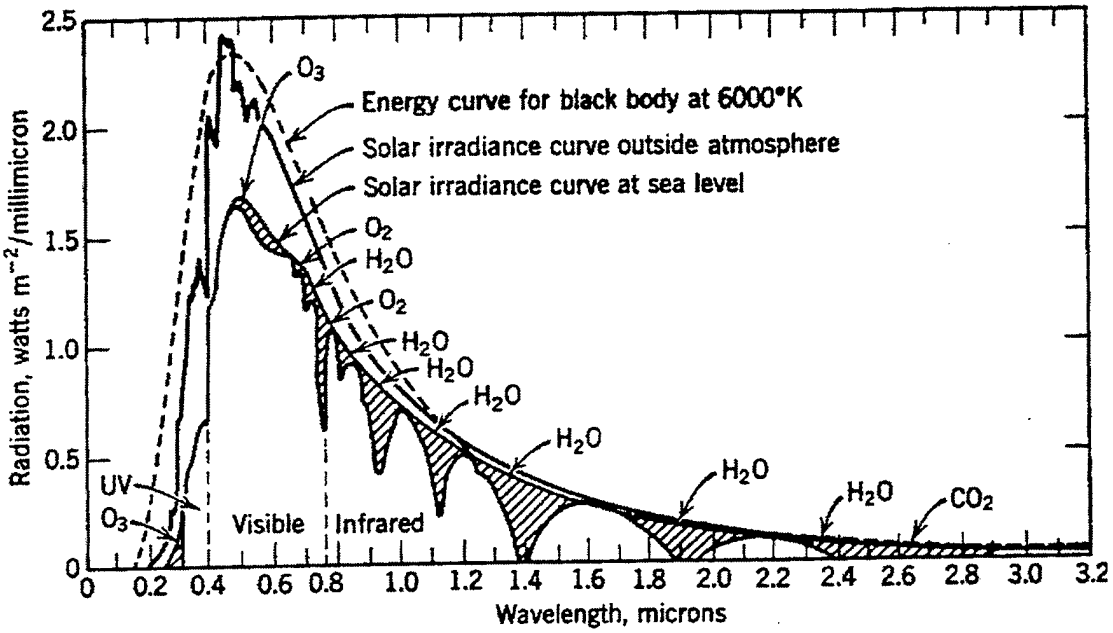

Figure IV-1. Solar spectra shown at various positions above the earth. [Handbook of Geophysics, The Macmillian Co.]

TECHNOLOGY OPERATIONS

The Aerospace Corporation functions as an "architect-engineer" for national security programs, specializing in advanced military space systems. The Corporation's Technology Operations supports the effective and timely development and operation of national security systems through scientific research and the application of advanced technology. Vital to the success of the Corporation is the technical staff's wide-ranging expertise and its ability to stay abreast of new technological developments and program support issues associated with rapidly evolving space systems. Contributing capabilities are provided by these individual Technology Centers:

Electronics Technology Center: Microelectronics, VLSI reliability, failure analysis, solid-state device physics, compound semiconductors, radiation effects, infrared and CCD detector devices, Micro-Electro-Mechanical Systems (MEMS), and data storage and display technologies; lasers and electro-optics, solid state laser design, micro-optics, optical communications, and fiber optic sensors; atomic frequency standards, applied laser spectroscopy, laser chemistry, atmospheric propagation and beam control, LIDAR/LADAR remote sensing; solar cell and array testing and evaluation, battery electrochemistry, battery testing and evaluation.

Mechanics and Materials Technology Center: Evaluation and characterization of new materials: metals, alloys, ceramics, polymers and composites; development and analysis of advanced materials processing and deposition techniques; nondestructive evaluation, component failure analysis and reliability; fracture mechanics and stress corrosion; analysis and evaluation of materials at cryogenic and elevated temperatures; launch vehicle fluid mechanics, heat transfer and flight dynamics; aerothermodynamics; chemical and electric propulsion; environmental chemistry; combustion processes; spacecraft structural mechanics, space environment effects on materials, hardening and vulnerability assessment; contamination, thermal and structural control; lubrication and surface phenomena; microengineering technology and microinstrument development.

Space and Environment Technology Center: Magnetospheric, auroral and cosmic ray physics, wave-particle interactions, magnetospheric plasma waves; atmospheric and ionospheric physics, density and composition of the upper atmosphere, remote sensing, hyperspectral imagery; solar physics, infrared astronomy, infrared signature analysis; effects of solar activity, magnetic storms and nuclear explosions on the earth's atmosphere, ionosphere and magnetosphere; effects of electromagnetic and particulate radiations on space systems; component testing, space instrumentation; environmental monitoring, trace detection; atmospheric chemical reactions, atmospheric optics, light scattering, state-specific chemical reactions and radiative signatures of missile plumes, and sensor out-of-field-of-view rejection.